A robust scheme for numerical simulation of heat transfer in two-fluid flows with high volumetric heat capacity contrasts

Min Lu, Zixuan Yang and Guowei He
Institute of Mechanics, Chinese Academy of Sciences, Beijing, China and School of Engineering Sciences, University of Chinese Academy of Sciences, Beijing, China

Received 17 May 2022
Revised 11 July 2022
18 July 2022
Accepted 18 July 2022

Abstract

Purpose – This paper aims to propose a new method for robust simulations of passive heat transfer in two-fluid flows with high volumetric heat capacity contrasts.

Design/methodology/approach – This paper implements a prediction–correction scheme to evolve the volumetric heat capacity. In the prediction substep, the volumetric heat capacity is evolved together with the temperature. The bounded downwind version of compressive interface capturing scheme for arbitrary meshes and central difference scheme are used for the spatial discretization of the advection and diffusion terms of the heat transfer equation, respectively. In the correction substep, the volumetric heat capacity is updated in accordance with the interface captured by using a coupled level-set and volume-of-fluid method to capture the interface dynamics precisely.

Findings – The proposed method is verified by simulating the advection of a hot droplet with high volumetric heat capacity, a stationary air–water tank with temperature variation between top and bottom walls and heat transfer during wave plunging at $Re = 10^8$. The test results show that the proposed method is practical and accurate for simulating two-fluid heat transfer problems, especially for those feature high volumetric heat capacity contrasts.

Originality/value – To ensure the numerical stability, this paper solves an additional conservative form of volumetric heat capacity equation along with the conservative form of temperature equation by using consistent spatial-discretization and temporal-integration schemes.

Keywords Heat transfer, Two-fluid flows, Wave breaking

Paper type Research paper

1. Introduction

Heat transfer in a two-fluid flow is ubiquitous in nature and industrial applications, such as water boiling (Yan and Li, 2006; Krause *et al.*, 2010), spray evaporations (Ernez and Morency, 2019), heat exchange between the ocean and atmosphere (Wan *et al.*, 2015) and combustion of liquid fuel (Wang *et al.*, 2020). In numerical studies of these problems, it is crucial to conduct robust and accurate simulations of heat transfer in two-fluid flows. There are tremendous two-fluid flow solvers based on the volume of fluid (VOF) method (Scardovelli and Zaleski, 1999), level-set (LS) method (Sussman *et al.*, 1994), front-tracking (FT) method (Unverdi and Tryggvason, 1992) and some other hybrid methods for capturing/tracking the interface between two fluid phases (Sussman and

This research is supported by the National Natural Science Foundation of China (NSFC) Basic Science Center Program for 'Multiscale Problems in Nonlinear Mechanics' (No.~11988102), NSFC project (No.~11972038), and Strategic Priority Research Program (Grant No.~XDB22040104).

International Journal of Numerical Methods for Heat & Fluid Flow

0961-5539
DOI 10.1108/HFF-05-2022-0296

Puckett, 2000; Aulisa *et al.*, 2003; Shin and Juric, 2009). Most previous works focused on problems with relatively low density contrast or at low to moderate Reynolds numbers due to the challenges in terms of both numerical robustness and accuracy to simulate two-phase flows with high density contrasts at a high Reynolds number (Scardovelli and Zaleski, 1999; Lörstad and Fuchs, 2004; Desjardins and Moureau, 2010; Arrufat *et al.*, 2020; Zhu and Masud, 2021). As such, numerical studies of heat transfer in two-fluid flows with high volumetric heat capacity contrasts are rather rarely reported in literature.

For two-fluid flows with high density contrasts (or at high Reynolds number), solving the conservative form of momentum equation is found to be the key to ensure the robustness of the simulation (Raessi and Pitsch, 2012). This is because the non-conservative form of governing equations do not exactly conserve the momentum, which induce unphysical momentum fluxes near the interface (Sussman *et al.*, 2007; Park *et al.*, 2009). Furthermore, in conventional FT or front-capturing methods, the density is determined by a marker function, which can be either the LS function, VOF function or indicator function constructed by front marker points. The evolution scheme of the marker function is usually different from the momentum equation. However, because the mass and momentum transfers take place simultaneously, any inconsistency in the numerical scheme can cause numerical errors that ultimately induce numerical instability, especially when the density contrast is high (Rudman, 1998). To overcome the inconsistency of fluxes between mass and momentum, Rudman (1998) proposes to calculate the momentum fluxes with the incorporation of the interface geometry. The interface-capturing scheme of Rudman (1998) is the VOF method. After that, by using a consistent scheme to discretize the VOF and momentum equations, Patel and Natarajan (2017) develops a robust numerical algorithm for simulating multiphase flows with high density contrasts. In the LS framework, Desjardins and Moureau (2010) calculate the momentum fluxes based on the value of the LS function and velocity to yield a tight coupling between LS and momentum transport equations. Raessi and Pitsch (2012) couple the mass and momentum by constructing flux densities from the LS function and used these densities to calculate the momentum fluxes. Another effective solution for the mass–momentum consistency problem is reported by Ghods and Herrmann (2013), where the density convection equation is solved by using a consistent scheme with the momentum equation. Recently, Nangia *et al.* (2019) develops a robust method for dynamically refined staggered Cartesian grids base on the idea of Ghods and Herrmann (2013). Also by solving the density convection equation, Zuzio *et al.* (2020) and Yang *et al.* (2021) extended the interface-capturing scheme to the coupled LS and VOF (CLSVOF) method in the framework of the consistent mass–momentum evolution. The advantages of different interface schemes are not the focus of this paper. We refer the readers to Tryggvason *et al.* (2011) and Scardovelli and Zaleski (1999) for more details.

Compared to the flow solver, there are less investigations on the numerical scheme for heat transfer in two-fluid flows with high volumetric heat capacity contrasts at high Reynolds numbers. For non-turbulent flows, the influence of bubble motion on the heat exchange rate between the liquid and a hot wall is studied by Deen and Kuipers (2013). The volumetric heat capacity ratio between gas and liquid is set to 1×10^{-2}. In Panda *et al.* (2019), the influence of the gas fraction on the wall-to-liquid heat transfer is analyzed, where the volumetric heat capacity ratio between gas and liquid ranges from 2×10^{-3} to 1.7×10^{-2}. In the studies of Nas *et al.* (2006) on the thermocapillary migration in both two-dimensional (2D) and three-dimensional (3D) flows, the volumetric heat

capacity ratio between gas and liquid is set to 0.25. To investigate the thermocapillary migration of drops with different fluid parameters, Yin and Li (2015) consider a low volumetric heat capacity ratio between the drop and background liquid, ranging from 0.2 to 2.5. For turbulent flows, numerical simulations of heat transfer in turbulent bubbly flows between two parallel walls with a constant heat flux are conducted by Dabiri and Tryggvason (2015). In their test cases, the volumetric heat capacity ratio between gas and liquid is set to 2×10^{-2}. In the numerical investigation of Tanaka (2011) on the heat transfer of a turbulent bubbly upflow in a vertical channel, the volumetric heat capacity ratio of gas and liquid ranges from 0.1 to 1.0.

Beyond the numerical studies of heat transfer in two-fluid flows reviewed above, many important problems are more challenging in terms of numerical robustness for two-fluid flows when the variation in volumetric heat capacity between the two fluids is large (e.g. the volumetric heat capacity ratio between air and water is 3×10^{-4}). Inspired by the mass–momentum consistency scheme for two-fluid flows with high density contrasts (Nangia *et al.*, 2019), we propose a robust scheme for numerical simulation of heat transfer in two-fluid flows based on the Computational Air-Sea Tank (CAS-Tank) (Yang *et al.*, 2021), in which the mass and momentum equations are discretized consistently using the high-resolution cubic upwind interpolation-based blending scheme (HR-CUIBS). To ensure the numerical robustness of solving the temperature field, an additional transport equation of volumetric heat capacity is solved along with the temperature equation. The bounded downwind version of compressive interface capturing scheme for arbitrary meshes (BD-CICSAM) is used to calculate the advection terms of temperature and volumetric heat capacity equations. For time marching, all of the transport equations are evolved consistently using the RK2 scheme. To examine the numerical robustness and accuracy, the proposed method is first verified by two cases without interface topology change. Specifically, the convection of a hot droplet with high volumetric heat capacity and a stationary air–water tank with temperature variation between top and bottom walls. To further verify the robustness of the proposed method in cases with violent interface topology changes, the heat transfer during wave plunging is simulated. The unfeasibility of using inconsistent schemes for both temporal and spatial discretization is emphasized through systematical tests. The rest of this paper is organized as follows. The numerical methods are detailed in Section 2. The numerical results are presented and discussed in Section 3. The conclusions are summarized in Section 4.

2. Formulation and numerical method

2.1 Governing equations

In the proposed method, a single set of equations is used for both liquid and gas phases, the continuity and momentum equations for the whole domain are as follows:

$$\nabla \cdot \mathbf{u} = 0, \tag{1}$$

$$\frac{\partial(\rho \mathbf{u})}{\partial t} + \nabla \cdot (\rho \mathbf{u}\mathbf{u}) = -\nabla p + \nabla \cdot 2\mu \mathbf{S} + \rho \mathbf{g} + \mathbf{f}_s, \tag{2}$$

where t is time, ρ and μ are, respectively, the fluid density and viscosity, p is the pressure, $\mathbf{u}$ is the velocity vector, $\mathbf{S}$ is the strain-rate tensor and $\mathbf{g}$ is the gravitational acceleration. The surface tension force $\mathbf{f}_s$ acting on the interface is defined as:

$$\mathbf{f}_s = \sigma\kappa\nabla H(\phi), \tag{3}$$

where σ is the surface tension coefficient, $\kappa = \nabla\cdot(\nabla\phi)$ at $\phi = 0$ is the curvature of the interface, in which ϕ represents the LS function. The Heaviside function $H(\phi)$ is defined as:

$$H(\phi) = \begin{cases} 0, & \phi \leq 0 \\ 1, & \phi > 0 \end{cases}. \tag{4}$$

We use the CLSVOF method to capture the liquid–gas interface. The transport equations of the LS function ϕ and VOF function ψ are expressed as:

$$\frac{\partial\phi}{\partial t} + \nabla\cdot(\phi\mathbf{u}) = 0, \tag{5}$$

$$\frac{\partial\psi}{\partial t} + \nabla\cdot(\psi\mathbf{u}) = 0. \tag{6}$$

Without loss of generality, we use "water" and "air" to represent two fluid phases in the following descriptions of this paper. The signed distance from grid points to the interface is described by the LS function ϕ, which is positively and negatively valued in water and air phases, respectively. The volume fraction of water in each grid cell is represented by the VOF function ψ, of which the value ranges from 0 to 1. An arbitrary fluid property η, which can be either the density ρ, kinematic viscosity μ, thermal conductivity coefficient k, or specific heat capacity c_p, is determined by the LS function as:

$$\eta = \eta_a + (\eta_w - \eta_a)H(\phi), \tag{7}$$

where the subscripts "a" and "w" represent air and water, respectively.

According to Patel and Natarajan (2017), Nangia *et al.* (2019) and Yang *et al.* (2021), the simulation is unstable with high density contrasts if the density is solely determined by equation (7). To construct a stable time-advancement scheme, the transport equation of density is given as:

$$\frac{\partial\rho}{\partial t} + \nabla\cdot\rho\mathbf{u} = 0. \tag{8}$$

The interface is precisely captured by equation (7) at the start of each time step, and meanwhile, the simulation is stable by evolving equation (8) to provide the density for the momentum equation within each time step.

To simulate the heat transfer in two-fluid flows, the following advection–diffusion equation is solved:

$$\frac{\partial\rho c_p\theta}{\partial t} + \nabla\cdot\rho c_p\theta\mathbf{u} = \nabla\cdot k\nabla\theta, \tag{9}$$

where θ represents the temperature. In the present study, we only consider the neutrally stratified condition, under which the physical properties remain constant in each fluid

phase. The phase change is not included. In other words, the temperature is treated as a passive scalar.

Similar to the flow solver, the solution of temperature is also unstable with high volumetric heat capacity contrasts, if ρc_p is determined solely using equation (7) (see the test results in Section 3.1). We follow the philosophy of mass–momentum consistent approach to develop a consistent numerical scheme for the transports of both temperature and volumetric heat capacity. For this purpose, the following convection equation of the volumetric heat capacity ρc_p is solved:

$$\frac{\partial \rho c_p}{\partial t} + \nabla \cdot \rho c_p \mathbf{u} = 0. \tag{10}$$

In each time step, equations (9) and (10) are evolved together. The evolution of equation (10) is called a prediction substep of the volumetric heat capacity, which ensures the simulation robustness by using consistent time-advancement and spatial-discretization schemes (see Sections 2.2 and 2.3) for the transport equations of temperature and volumetric heat capacity. However, ρc_p is not coupled to the interface geometry in the prediction substep. After the full-step evolution of equations (9) and (10), ρc_p is corrected using equation (7) to give an initial value for the next time step. The correction substep provides a more accurate representation of the interface geometry by incorporating the LS function.

The momentum equation is solved using the CAS-Tank developed by Yang *et al.* (2021), in which the mass–momentum consistency scheme was adopted to calculate the velocity field. Specifically, the RK2 scheme is used to advance the transport equations of mass and momentum with their advection terms being discretized by HR-CUIBS. We refer the readers to Yang *et al.* (2021) for more details of the momentum solver. Below, we focus on the temporal advancement and spatial discretization of the temperature field.

2.2 Time advancement

For notational simplicity, the volumetric heat capacity ρc_p is replaced by ξ hereinafter. At the start of time step n, the volumetric heat capacity ξ^n is computed by equation (7). Then, the volumetric heat capacity and temperature are advanced as:

$$\xi^{(1)} = \xi^{(0)} - \left[\nabla \cdot \left(\xi^{(0)}\mathbf{u}^{(0)}\right)\right]\Delta t, \tag{11}$$

$$\xi^{(2)} = \xi^{(1)} - \frac{1}{2}\left[\nabla \cdot \left(\xi^{(1)}\mathbf{u}^{(1)}\right) - \nabla \cdot \left(\xi^{(0)}\mathbf{u}^{(0)}\right)\right]\Delta t, \tag{12}$$

$$\xi^{(1)}\theta^{(1)} = \xi^{(0)}\theta^{(0)} - \left[\nabla \cdot \left(\xi^{(0)}\theta^{(0)}\mathbf{u}^{(0)}\right) - \nabla \cdot \left(k\nabla\theta^{(0)}\right)\right]\Delta t, \tag{13}$$

$$\xi^{(2)}\theta^{(2)} = \xi^{(1)}\theta^{(1)} - \frac{1}{2}\left\{\left[\nabla \cdot \left(\xi^{(1)}\theta^{(1)}\mathbf{u}^{(1)}\right) - \nabla \cdot \left(k\nabla\theta^{(1)}\right)\right] - \left[\nabla \cdot \left(\xi^{(0)}\theta^{(0)}\mathbf{u}^{(0)}\right) - \nabla \cdot \left(k\nabla\theta^{(0)}\right)\right]\right\}\Delta t. \tag{14}$$

Here, the substeps of the RK2 method are denoted by superscripts "(1)" and "(2)", while superscripts "(0)" and "(2)" also represent variables at steps n and $(n + 1)$, respectively. The Courant–Friedrichs–Lewy (CFL) number is used to adjust the time step Δt dynamically as:

$$\Delta t = CFL \cdot \min\left\{\frac{\Delta_x}{u}, \frac{\Delta_y}{v}, \frac{\Delta_z}{w}, \frac{\rho\Delta^2}{6\mu}, \frac{\rho C_p\Delta^2}{6k}, \sqrt{\frac{\Delta}{g}}, \sqrt{\frac{\rho\Delta^3}{2\pi\sigma}}\right\}, \tag{15}$$

where Δ_x, Δ_y and Δ_z are the distances between two grid points in x-, y- and z-directions, respectively, and the characteristic distance is defended as $\Delta = (\Delta_x\Delta_y\Delta_z)^{1/3}$.

We note that the RK2 scheme can be replaced by any time advancement scheme. The key point is that the time advancement schemes for equations (9) and (10) are consistent. On the opposite, if equations (9) and (10) are advanced using different time schemes, the solver is unstable. We show this point in Section 3.1.

2.3 Discretization of advection terms

A finite difference scheme is used for spatial discretization. A staggered Cartesian grid is used to define the flow quantities. The velocity vector components are discretized at cell faces, while other scalar quantities are defined at cell centers, i.e. the density ρ, viscosity μ, pressure p, temperature θ, volumetric heat capacity ξ, thermal conductivity κ, LS function ϕ and VOF function ψ. We set x_i, y_j, and z_k as the discretized coordinates with $i = 1, 2,\ldots,N_x$, $j = 1,2,3,\ldots, N_y$, and $k = 1,2,3,\ldots, N_z$ being the quantities defined at cell centers. Here, N_x, N_y, and N_z are the number of grid points in x-, y- and z-direction, respectively.

At the start of each time step, the volumetric heat capacity ξ^n and thermal conductivity coefficient k^n are calculated using equation (7). To obtain $\xi^{(1)}$ and $\xi^{(2)}$ in equations (11) and (12), respectively, the advection term is discretized as:

$$\begin{aligned}-[\nabla\cdot(\xi\mathbf{u})]_{i,j,k} = &-\frac{\tilde{\xi}_{i+1/2,j,k}u_{i+1/2,j,k} - \tilde{\xi}_{i-1/2,j,k}u_{i-1/2,j,k}}{\Delta_x}\\ &-\frac{\tilde{\xi}_{i,j+1/2,k}v_{i,j+1/2,k} - \tilde{\xi}_{i,j-1/2,k}v_{i,j-1/2,k}}{\Delta_y}\\ &-\frac{\tilde{\xi}_{i,j,k+1/2}w_{i,j,k+1/2} - \tilde{\xi}_{i,j,k-1/2}w_{i,j,k-1/2}}{\Delta_z},\end{aligned} \tag{16}$$

where $\tilde{\xi}$ at cell face is calculated using the third-order total variation diminishing scheme. Taking the calculation of $\tilde{\xi}_{i-1/2,j,k}$ as an example, the stencil points needed in the scheme are selected according to the sign of the velocity at cell face $u_{i-1/2,j,k}$, as:

$$(\xi_u, \xi_c, \xi_d) = \begin{cases}(\xi_{i-2,j,k}, \xi_{i-1,j,k}, \xi_{i,j,k}), u_{i-1/2,j,k} \geq 0\\ (\xi_{i+1,j,k}, \xi_{i,j,k}, \xi_{i-1,j,k}), u_{i-1/2,j,k} < 0\end{cases}, \tag{17}$$

where subscripts "u", "c", and "d" denote the grid points positioned far upwind, upwind and downwind, respectively. The volumetric heat capacity at an arbitrary cell face is expressed as:

$$\tilde{\xi} = \xi_c + \frac{(\xi_c - \xi_u)}{2}\gamma(r), \tag{18}$$

where $\gamma(r)$ represents the flux limiter, which is determined by BD-CICSAM scheme as:

$$\gamma(r) = \max\{0, \min[2r, 2(Co^{-1} - 1)]\}, \tag{19}$$

where Co is the Courant number, and the ratio of centered to upwind gradient r is defined as:

$$r = \frac{\xi_d - \xi_c}{\xi_c - \xi_u}. \tag{20}$$

More details about the interpolation scheme can be found in Ubbink and Issa (1999). We note here that in Yang *et al.* (2021), the advection terms in the momentum equation are discretized using the HR-CUIBS. We choose a different scheme, namely the BD-CICSAM scheme, to discretize the advection term of the heat transfer equation because it is less diffusive, resulting in a smaller numerical error. This point is further shown in Section 3.1.

The spatial discretization of $\nabla\cdot(\xi\theta\mathbf{u})$ in equations (13) and (14) is written as:

$$\begin{aligned} -[\nabla\cdot(\xi\theta\mathbf{u})]_{i,j,k} = &-\frac{\tilde{\xi}_{i+1/2,j,k}\tilde{\theta}_{i+1/2,j,k}u_{i+1/2,j,k} - \tilde{\xi}_{i-1/2,j,k}\tilde{\theta}_{i-1/2,j,k}u_{i-1/2,j,k}}{\Delta_x} \\ &-\frac{\tilde{\xi}_{i,j+1/2,k}\tilde{\theta}_{i,j+1/2,k}v_{i,j+1/2,k} - \tilde{\xi}_{i,j-1/2,k}\tilde{\theta}_{i,j-1/2,k}v_{i,j-1/2,k}}{\Delta_y} \\ &-\frac{\tilde{\xi}_{i,j,k+1/2}\tilde{\theta}_{i,j,k+1/2}w_{i,j,k+1/2} - \tilde{\xi}_{i,j,k-1/2}\tilde{\theta}_{i,j,k-1/2}w_{i,j,k-1/2}}{\Delta_z}. \end{aligned} \tag{21}$$

A second-order central difference scheme is used to discretize the diffusion terms in equations (13) and (14), namely:

$$\begin{aligned} [\nabla\cdot(k\nabla\theta)]_{i,j,k} = &\frac{k_{i+1/2,j,k}\left(\frac{\partial\theta}{\partial x}\right)_{i+1/2,j,k} - k_{i-1/2,j,k}\left(\frac{\partial\theta}{\partial x}\right)_{i-1/2,j,k}}{\Delta_x} \\ &+\frac{k_{i,j+1/2,k}\left(\frac{\partial\theta}{\partial y}\right)_{i,j+1/2,k} - k_{i,j-1/2,k}\left(\frac{\partial\theta}{\partial y}\right)_{i,j-1/2,k}}{\Delta_y} \\ &+\frac{k_{i,j,k+1/2}\left(\frac{\partial\theta}{\partial z}\right)_{i,j,k+1/2} - k_{i,j,k-1/2}\left(\frac{\partial\theta}{\partial z}\right)_{i,j,k-1/2}}{\Delta_z}. \end{aligned} \tag{22}$$

Here, we used the interpolation scheme reported by Liu *et al.* (2000) to calculate the thermal conductivity k of cell faces in the vicinity of the interface. Assuming that the interface lies between nodes i and $i + 1$ in the x-direction, the value of k at the cell face $i + 1/2$ can be estimated more accurately by using a height function φ, defined as:

$$\varphi = \frac{|\phi_i|}{|\phi_i| + |\phi_{i+1}|}, \tag{23}$$

where ϕ is the LS function. The thermal conductivity $k_{j+1/2}$ at the cell face is given as a weighted harmonic averaging of the values of k at two neighboring cell centers, namely:

$$k_{i+1/2,j,k} = \frac{k_{i,j,k}k_{i+1,j,k}}{\varphi k_{i+1,j,k} + (1-\varphi)k_{i,j,k}}. \tag{24}$$

Through the use of the thermal conductivity $k_{i+1/2,j,k}$ at cell faces determined by equations (23) and (24), the numerical solution converges to the analytical solution in a second-order accuracy (see Section 3.2). The temperature gradient $\nabla\theta$ in equation (22), taking $\partial\theta/\partial x$ as an example, is calculated as:

$$\left(\frac{\partial\theta}{\partial x}\right)_{i+1/2,j,k} = \frac{\theta_{i+1,j,k} - \theta_{i,j,k}}{\Delta_x}. \tag{25}$$

2.4 Temperature boundary conditions

The boundary condition for the temperature field can be either prescribed value of temperature gradient, prescribed value of temperature or periodic. The boundary condition in the x-direction is used to demonstrate the implementation. To construct the BD-CICSAM interpolation scheme on boundaries, two ghost cells are needed along each domain boundary. In other words, the implementation of temperature boundary condition is to calculate the values of temperature θ for $i = 0$ and -1. If the temperature gradient is prescribed as B at the boundary, the temperature in the ghost cell is given as:

$$\begin{cases} \theta_{0,j,k} = \theta_{1,j,k} - B(x_{1,j,k} - x_{0,j,k}); \theta_{-1,j,k} = \theta_{2,j,k} - B(x_{2,j,k} - x_{-1,j,k}) \\ \theta_{Nx+1,j,k} = \theta_{Nx,j,k} + B(x_{Nx+1,j,k} - x_{Nx,j,k}); \theta_{Nx+2,j,k} = \theta_{Nx-1,j,k} + B(x_{Nx+2,j,k} - x_{Nx-1,j,k}) \end{cases}. \tag{26}$$

If the temperature is prescribed as C, the boundary condition is expressed as:

$$\begin{cases} \theta_{0,j,k} = 2C - \theta_{1,j,k}; \theta_{-1,j,k} = 2C - \theta_{2,j,k} \\ \theta_{Nx+1,j,k} = 2C - \theta_{Nx,j,k}; \theta_{Nx+2,j,k} = 2C - \theta_{Nx-1,j,k} \end{cases}. \tag{27}$$

Here, C is wall temperature. The periodic boundary condition is defined as:

$$\begin{cases} \theta_{-1,j,k} = \theta_{Nx-1,j,k}; \theta_{0,j,k} = \theta_{Nx,j,k} \\ \theta_{Nx+1,j,k} = \theta_{1,j,k}; \theta_{Nx+2,j,k} = \theta_{2,j,k} \end{cases}. \tag{28}$$

The implementation of temperature boundary condition in other directions can be deduced accordingly.

3. Result

3.1 Convection of a hot droplet with high volumetric capacity

In this section, we present the test results of the convection of a hot droplet with high volumetric heat capacity. The computational domain and initial condition of this test case is depicted in Figure 1. A 2D high-volumetric-heat-capacity droplet with higher temperature $\theta = 1$ is surrounded by low-density ambient fluid with lower temperature $\theta = 0$. The volumetric heat capacities of the droplet and ambient fluid are 4×10^6 and 1, respectively. The thermal conductivity k, viscosity μ, gravitational acceleration $\mathbf{g}$, and surface tension

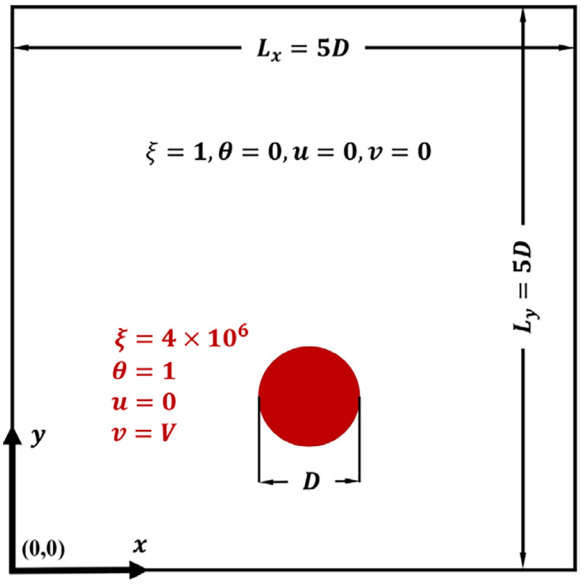

Figure 1.
Schematic of the computational domain and initial setup for the numerical simulation of the convection of a hot droplet with high volumetric heat capacity

$\mathbf{f}_s$ are neglected in this test case. Initially, the droplet has a constant vertical velocity V, while the ambient fluid remains still. The hot droplet is expected to move steadily without any heat exchange with the ambient fluid. This canonical case was used to test the numerical robustness and accuracy of the flow solver (Nangia *et al.*, 2019; Yang *et al.*, 2021), and the performance of the flow solver for the present test case is detailed in Yang *et al.* (2021). In this paper, we focus on the verification of the temperature solver described in Section 2. The computational domain is $5D \times 5D$ in both x- and y-directions with D being the droplet diameter. The origin of the coordinates is in the lower left corner of the computational domain. The droplet center is initially located at $(x, y) = (2.5D, 1.5D)$. The boundary conditions in the x-direction for velocity and temperature are no-slip and adiabatic, respectively. Periodic boundary conditions are set in the y-direction for both velocity and temperature fields. The number of grid points is fixed to $N_x \times N_y = 128 \times 128$, which is sufficient to make an accurate simulation of the droplet motion according to Yang *et al.* (2021).

Figure 2 shows the contours of temperature and droplet positions at $t = 0.1T$, $0.4\,T$, $0.7\,T$ and $1.0\,T$, where $T = 5D/V$ is the period for the droplet to return to its original position. The droplet interface is shown using the black solid line, whereas the color contours represent the temperature distribution. As is noted in Section 2.3, we have tested two different spatial discretization schemes for the advection term of the heat transfer equation, namely, the BD-CICSAM scheme and the HR-CUIBS scheme. The HR-CUIBS scheme is also used to discretize the advection term of the momentum equation. It is seen that the temperature inside the droplet remains almost unchanged based on both spatial discretization schemes. This observation is desired. The air in the wake of the droplet is slightly heated. This is caused by the numerical diffusion of the spatial discretization scheme, which is not completely avoidable, but can be reasonably reduced by choosing an appropriate spatial discretization scheme for the advection term. From the comparison between Figures 2(d) and 2(h), it is evident that the BD-CICSAM scheme is numerically less diffusive, and as such the

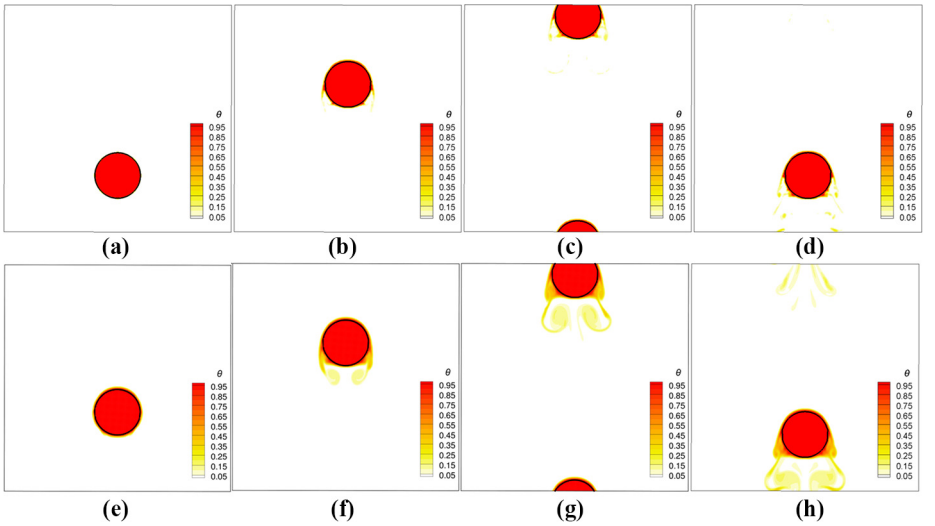

Figure 2.
Contours of temperature and interface positions for numerical simulations of the convection of a hot droplet with high volumetric heat capacity at (a,e) $t = 0.1T$, (b,f) $t = 0.4T$, (c,g) $t = 0.7T$ and (d,h) $t = 1.0T$

Notes: The results in (a)-(d) are obtained using the BD-CICSAM scheme for spatial discretization of the advection term of the heat transfer equation, while in (e)-(h), the HR-CUIBS scheme is used. The computational domain is discretized using 128 × 28 number of grid points

artificial heat flux across the droplet interface shown in Figure 2(d) is less significant than that in Figure 2(h). To quantify the numerical accuracy, we define the error in the temperature field as:

$$E = \frac{1}{L_x L_y} \sum_{i=1}^{N_x} \sum_{j=1}^{N_y} |(\theta - \theta_0)_{i,j}| \Delta_x \Delta_y, \tag{29}$$

where θ_0 denotes the theoretical solution of temperature, which is 1 and 0 inside and outside the droplet, respectively. The evolution of the bulk error E in temperature from different cases with various advection schemes are shown in Figure 3. It is seen that although the error accumulates in both cases, the performance of BD-CICSAM scheme is more satisfactory. We note that the advection term of the momentum and mass equation is discretized consistently by HR-CUIBS scheme. This is because the BD-CICSAM scheme causes numerical instability in the momentum solver (not shown), though the numerical diffusion is less than the HR-CUIBS. The satisfactory results shown in Figures 2(a)–(d) also indicates that the advection scheme for the transport equations of momentum and mass is not required to be strictly consistent with those of temperature and volumetric heat capacity. The investigation of different finite differential scheme is not the focus of this paper. In general, a differential scheme with less numerical diffusion is usually more unstable, and the choice of the differential scheme should be case dependent. In the present study, we choose the BD-CICSAM scheme because they are stable in all cases.

The above test shows that the temperature solver introduced in Section 2 is robust for the simulation of the convection of a hot droplet with high volumetric heat capacity, whereas the numerical diffusion is associated with the discretization scheme. Solving a non-conservative

form of the temperature equation can possibly reduce the numerical error. As such, we have run the same case by solving the non-conservative form of temperature equation, which is given as:

$$\rho c_p \left(\frac{\partial \theta}{\partial t} + \mathbf{u} \cdot \nabla \theta \right) = 0, \tag{30}$$

and discretized as:

$$\begin{aligned} \theta_{i,j,k}^{n+1} = \theta_{i,j,k}^{n} - \Delta t \Bigg[& \left(\frac{u_{i+1/2,j,k}^{n} + u_{i-1/2,j,k}^{n}}{2} \right) \left(\frac{\tilde{\theta}_{i+1/2,j,k}^{n} + \tilde{\theta}_{i-1/2,j,k}^{n}}{\Delta x} \right) \\ & + \left(\frac{v_{i,j+1/2,k}^{n} + v_{i,j-1/2,k}^{n}}{2} \right) \left(\frac{\tilde{\theta}_{i,j+1/2,k}^{n} + \tilde{\theta}_{i,j+1/2,k}^{n}}{\Delta y} \right) \\ & + \left(\frac{w_{i,j,k+1/2}^{n} + w_{i,j,k-1/2}^{n}}{2} \right) \left(\frac{\tilde{\theta}_{i,j,k+1/2}^{n} + \tilde{\theta}_{i,j,k-1/2}^{n}}{\Delta z} \right) \Bigg]. \end{aligned} \tag{31}$$

The temperature contours at early stage of the simulation ($t = 0.1T$) is shown in Figure 4(a). It is seen that the temperature at the wake of the droplet is negative, which is physically incorrect. Evidently, this unphysical temperature is associated with the non-conservative form of equation. The time evolutions of the integral error of temperature E is depicted in Figure 4(b). The time evolution of E obtained from solving conservative form of temperature equation is also superimposed for comparison. It is evident that the integral error of temperature for the non-conservative equation is greater than that for the conservative equation at the end of the simulation, and the oscillation in the error indicates the numerical instability. This issue of the non-conservative scheme leads to the divergence of the simulation for problems with complex interface geometries as shown in Sec. 3.3. To further

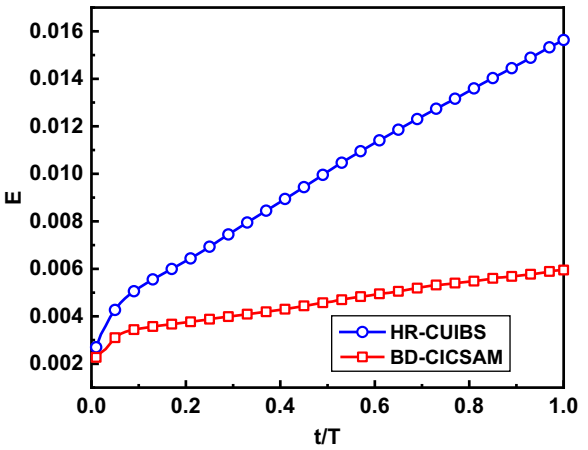

Figure 3.
Evolution of the bulk error E in temperature for the simulations of the convection of a droplet with high volumetric heat capacity obtained from different simulations with various spatial discretization schemes for the advection terms in the temperature and volumetric heat capacity equations

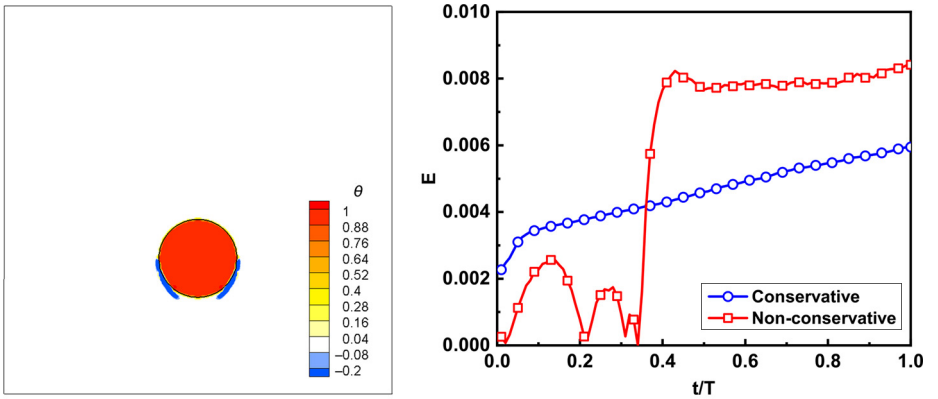

Figure 4.
Numerical result obtained from solving the non-conservative form of temperature equation for the simulation of a hot droplet with high volumetric heat capacity

Notes: (a) Temperature fields at t = 0.1T; (b) The evolution of the integral error of temperature E. The result obtained from solving conservative form of temperature equation is superimposed for comparison

show the difference between the calculation of temperature field using the numerical algorithm introduced in Section 2 and equation (31), the discretized form of equation (9) is given for comparison as:

$$\theta_{i,j,k}^{n+1} = \frac{\tilde{\xi}_{i,j,k}^{n}\theta_{i,j,k}^{n}}{\tilde{\xi}_{i,j,k}^{n+1}} - \frac{\Delta t}{\tilde{\xi}_{i,j,k}^{n+1}}\left[\left(\frac{u_{i+1/2,j,k}^{n}\tilde{\xi}_{i+1/2,j,k}^{n}\tilde{\theta}_{i+1/2,j,k}^{n} + u_{i-1/2,j,k}^{n}\tilde{\xi}_{i-1/2,j,k}^{n}\tilde{\theta}_{i-1/2,j,k}^{n}}{\Delta x}\right)\right.$$
$$+\left(\frac{v_{i,j+1/2,k}^{n}\tilde{\xi}_{i,j+1/2,k}^{n}\tilde{\theta}_{i,j+1/2,k}^{n} + v_{i,j-1/2,k}^{n}\tilde{\xi}_{i,j+1/2,k}^{n}\tilde{\theta}_{i,j+1/2,k}^{n}}{\Delta y}\right) \quad (32)$$
$$\left.+\left(\frac{w_{i,j,k+1/2}^{n}\tilde{\xi}_{i,j,k+1/2}^{n}\tilde{\theta}_{i,j,k+1/2}^{n} + w_{i,j,k-1/2}^{n}\tilde{\xi}_{i,j,k-1/2}^{n}\tilde{\theta}_{i,j,k-1/2}^{n}}{\Delta z}\right)\right],$$

where $\tilde{\xi}_{i,j,k}^{n+1}$ is calculated by solving the discretized form of equation (10) as:

$$\xi_{i,j,k}^{n+1} = \xi_{i,j,k}^{n} - \Delta t\left[\left(\frac{u_{i+1/2,j,k}^{n}\tilde{\xi}_{i+1/2,j,k}^{n} + u_{i-1/2,j,k}^{n}\tilde{\xi}_{i-1/2,j,k}^{n}}{\Delta x}\right)\right.$$
$$\left.+\left(\frac{v_{i,j+1/2,k}^{n}\tilde{\xi}_{i,j+1/2,k}^{n} + v_{i,j-1/2,k}^{n}\tilde{\xi}_{i,j+1/2,k}^{n}}{\Delta y}\right) + \left(\frac{w_{i,j,k+1/2}^{n}\tilde{\xi}_{i,j,k+1/2}^{n} + w_{i,j,k-1/2}^{n}\tilde{\xi}_{i,j,k-1/2}^{n}}{\Delta z}\right)\right]. \quad (33)$$

It is evident from equation (32) that the calculation of the temperature equation at $n + 1$ should consider the values of volumetric heat capacity at the cell faces when the governing equation is employed in conservative form. As such, although equations (9) and (30) are equivalent, their discretized form, i.e. equations (32) and (31) are inequivalent for the following reasons. First, the divergence-free condition is not satisfied strictly, due to the residual in the Poisson equation. Second, the discretized form of equations (32) and (31) are

also inequivalent due to the different values of volumetric heat capacity in different phases. Under an overall consideration of the accuracy and numerical robustness, we choose to solve the conservative form of governing equation considering that in a two-fluid flow, heat ($\xi\theta$) is a conservative variable, but temperature (θ) is not.

As noted in Section 2.1, the consistency in the spatial discretization schemes for the advection terms of the transport equations of the temperature and volumetric heat capacity is crucial for sustaining the numerical stability. To show this point, we use BD-CICSAM and upwind schemes to discretize the advection terms of the temperature and volumetric heat transport equations, respectively. The simulation is found to be unstable, and Figure 5(a) shows the contours of temperature at $t = 0.75T$ before the simulation diverges. It is observed that a very high temperature region occurs at the edge of droplet, which is physically incorrect. Furthermore, it is a natural choice to use the position of the interface at time step $(n + 1)$ to determine the values of ξ^{n+1} through equation (7). After conducting a test, we find that this choice of ξ^{n+1} also leads to an unstable simulation for the present case with high volumetric heat capacity contrast. The temperature contours at $t = 0.2T$ for this test are shown in Figure 5(b). It is seen that unphysically high temperature also occurs near the droplet interface. However, we also note here that using interface position to obtain the ξ^{n+1} can deal with problems with low volumetric heat capacity contrast of $O(1)$ (Lu *et al.*, 2019). This point can be shown using a test with a volumetric heat capacity ratio of 1.1. The temperature contours for this test are shown in Figure 5(c). It is seen that the result of temperature is reasonable.

Next, we show the importance of the consistency in time advancement scheme when evolving the temperature and volumetric heat capacity transport equations. To this end, we have conducted three test cases with different time advancement strategies. In the first and second cases, consistent time advancement schemes are used. Specifically, the RK2 scheme is used in the first case and the forward Euler scheme is used in the

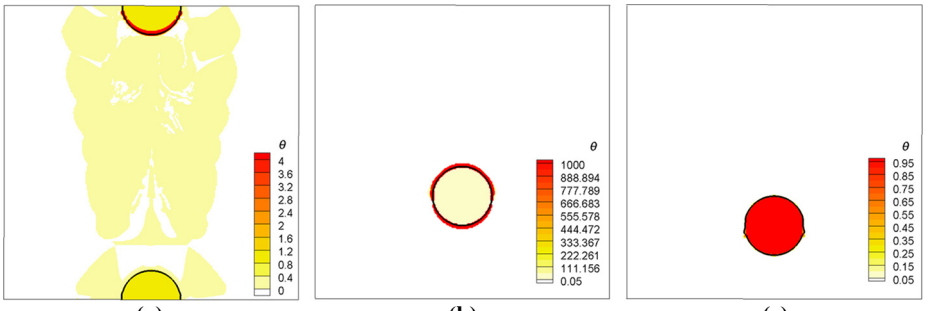

(a) (b) (c)

Figure 5. Contours of temperature for the simulation of the convection of a hot droplet with high volumetric heat capacity obtained from inconsistent spatial discretization schemes for the advection terms of the transport equations of the temperature and volumetric heat capacity

Notes: (a) BD-CICSAM and upwind schemes are used to discretize the advection terms of the transport equations of temperature and volumetric heat capacity, respectively; (b) and (c) BD-CICSAM scheme is used to discretize the advection term of the transport equation of temperature, while the volumetric heat capacity is determined using the interface position as given by Eq. (7). The volumetric heat capacity ratio between the droplet and air is (a, b) 4×10^6 and (c) 1.1. The simulations for panels (a) and (b) are unstable. Specifically, the result at t = 0.75T and 0.2T are shown in panel (a) and (b), respectively. The simulation for panel (c) is stable, and the result at t = 1.0T is shown

second one to evolve the transport equations of both temperature and volumetric heat capacity. In the third case, the transport equations of temperature and volumetric heat capacity are evolved using inconsistent schemes, i.e. RK2 and forward Euler schemes for the transport equations of temperature and volumetric heat capacity, respectively. The results of these three test cases are compared in Figure 6. It is seen that the temperature solver is stable if the temperature and volumetric heat capacity transport equations are advanced using consistent schemes, either RK2 or first-order forward Euler scheme. However, as shown in Figure 6(c), if inconsistent schemes are used to evolve the temperature and volumetric heat capacity, the solution of temperature field diverges.

3.2 Stationary air–water tank with temperature variation between top and bottom walls

This test case is conducted to examine the accuracy of the diffusion term in the temperature transport equation. Below is the description of the numerical setup. The size of the computational domain is $L_x \times L_y = L \times L$. As shown in Figure 7, the lower half of the domain is filled with water, while the remainder of the domain is air. The velocity is prescribed to be zero. The thermal conductivity ratio between air and water is 3.85×10^{-2}. The temperature is fixed at 1 and 0 at the top and bottom walls, respectively, and a homogenous heat source $q = -1$ is added in the entire domain. In the horizontal (x −) direction, a periodic boundary condition is applied. Because the fluid remains still, and the temperature is fixed at the top and bottom walls, the solution of temperature ultimately converges to a steady state. The analytical solution can be written as:

$$\theta = \begin{cases} 0.5000y^2 - 0.6573y & 0 \le y \le L/2 \\ 12.9870y^2 - 17.0727y + 5.0857 & L/2 < y \le L \end{cases}, \tag{34}$$

which is a quadratic function of y. Figure 8 compares the numerical results of this test case obtained from different number of grid points with the analytical solution. Figure 8(a) shows that the numerical error mainly occurs near the interface and the numerical result also converges to the analytical solution as the number of grid points increases. To quantify the

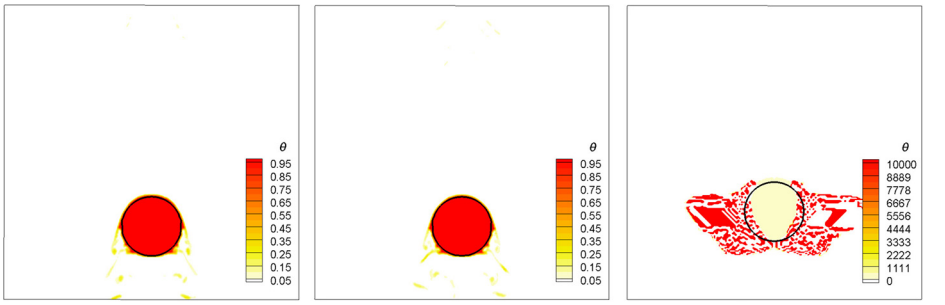

Figure 6.
Temperature fields for the simulation of a hot droplet with high volumetric heat capacity obtained from different time advancement strategies

Notes: (a) RK2 scheme for both temperature and volumetric heat capacity (t = 1.0T); (b) Forward Euler scheme for both temperature and volumetric heat capacity (t = 1.0T)); (c) RK2 and forward Euler schemes for temperature and volumetric heat capacity transport equations (t = 0.05T), respectively

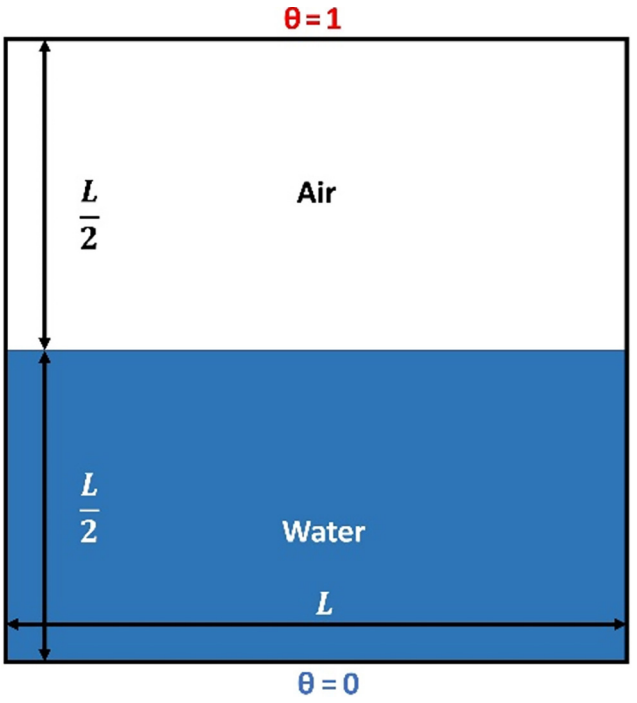

Figure 7.
Computational domain of the stationary air–water tank with temperature variation between top and bottom walls

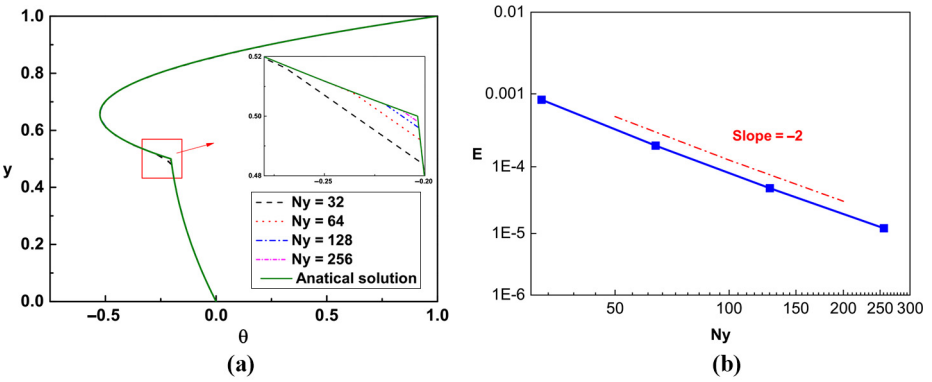

Figure 8.
Numerical results for the test case of the stationary air–water tank with temperature variation between top and bottom walls with constant heat source

Notes: (a) Vertical profiles of temperature at steady state; (b) the numerical error E as a function of the number of grid points in y-direction N_y

accuracy, the error in the temperature E as a function of the grid points in the y-direction (N_y) is depicted in Figure 8(b). Here, the definition of the error is also given by equation (30) with θ_0 being the analytical solution. It is evident from Figure 8(b) that the accuracy of the numerical solution reaches the second order.

3.3 Temperature transfer during wave plunging

Thus far, the temperature solver is tested using 2D cases without interface topology change. To further verify the numerical robustness of the proposed method in the problems with violent interface topology changes, we simulate the temperature transfer during wave plunging. The independent non-dimensional parameters include the Reynolds number $Re = \lambda^{3/2} g^{1/2}/\nu_w = 2.46 \times 10^8$, Bond number $Bo = \rho_w g \lambda^2/\sigma = 5.4 \times 10^7$, and Prandtl number $Pr = c_{p_w} \mu_w / k_w = 7.01$, where λ is the wave length. The volumetric heat capacity ratio and thermal conductivity coefficient ratio between air and water are 3×10^{-4} and 3.85×10^{-2}, respectively. Figure 9 shows the computational domain. The wave geometry is initially prescribed as a third-order Stokes wave. The wave travels in the $+x$-direction, and the vertical direction is denoted by y. The mean elevation of water is located at $y = 0$. To generate a plunging breaker, we set the initial wave steepness to $\varepsilon_0 = ka_0 = 0.55$, where a_0 is the amplitude of the initial wave and $k = 2\pi/\lambda$ is the wavenumber. The mean water depth is $h = \lambda/2$, and the dispersion parameter $kh = \pi$ corresponds to a deep-water condition (Mei, 1989). The size of computational domain is $L_x \times L_y = \lambda \times \lambda$, discretized using $N_x \times N_y = 512 \times 512$ grid points. The periodic boundary condition is set in the horizontal direction for both velocity and temperature fields, while the free-slip and prescribed temperature conditions are applied at top and bottom walls. We note that this test case has been validated in an isothermal environment, and the numerical robustness of the momentum solver is detailed in Yang *et al.* (2021). In present study, we focus on the numerical robustness of the proposed temperature solver.

We have conducted both 2D and 3D cases. The 2D case is conducted to examine the performance the conservative and non-conservative form of temperature equations. The successive snapshots of the interface geometries and contours of temperature field of $2D$ results obtained from solving the conservative form of temperature equation are depicted in

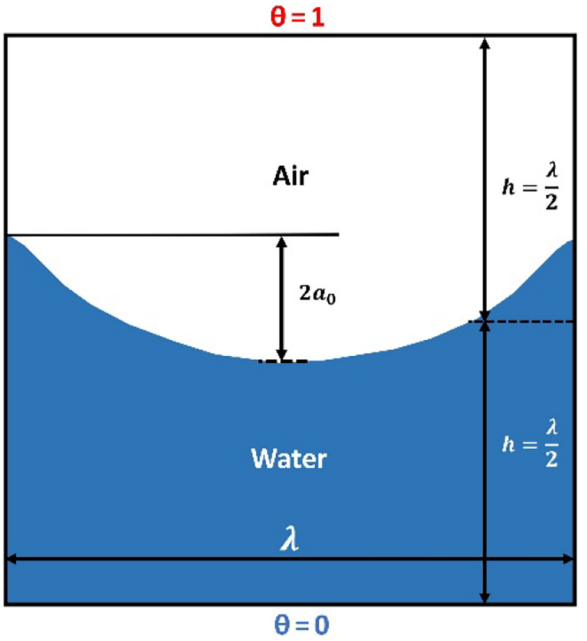

Figure 9.
Schematic of the computational domain and initial setup for the simulation of heat transfer during wave plunging

Figure 10. It is seen that both the interface and the temperature field are reasonably resolved. However, the numerical results diverge at the early stage of the simulation when the non-conservative form of temperature equation is employed. This is shown in Figure 11, in which the evolution of bulk mean temperature is depicted. This test case shows that solving the non-conservative form of the temperature equation is unstable for problems with complex interface geometries and violent wave breaking events.

In the 3D case, the spanwise domain size is set to $L_z = 0.25\lambda$, discretized using $N_z = 128$ homogeneously distributed grid points. A periodic condition is applied in the spanwise direction. Other parameters remain the same as the 2D case. Figure 12 shows the successive snapshots of the air-water interface and the contours of temperature in a cross-sectional plane at $z = 0$. As shown, the wave front is steepened at $t = 0.5T$ [Figure 12(a)] and the temperature isopleths become distorted over the wave crest. At $t = 1.0T$ [Figure 12(b)], an overturning jet is observed and the temperature on the back of the jet is further mixed due to the vortex generated there. After the overturning jet impinges onto the water surface at $t = 2.0T$, the temperature mixing is further enhanced on the air side [Figure 12(c)]. As the wave continues to break, the heat transfer on the water side is also enhanced [Figure 12(d)]. After that, the wave breaking calms down but continues to propagate with the temperature being further mixed as shown in Figures 12(e) and (f).

The time evolution of the bulk mean temperature of air obtained from $2D$ and $3D$ simulations are compared in Figure 13. It is observed that the bulk mean temperature of air

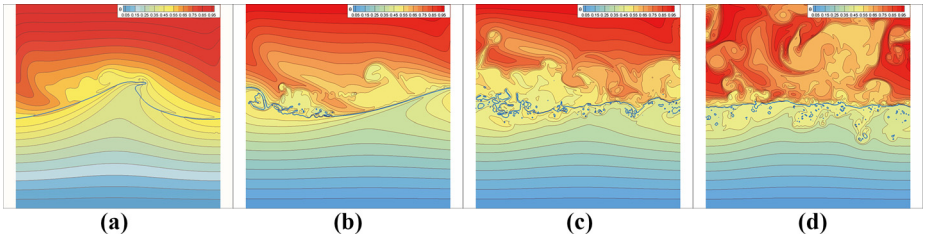

Figure 10. Wave geometry (thick blue line) and isopleths of temperature (thin grey lines) at (a) $t = 1T$, (b) $t = 2T$, (c) $t = 4T$ and (d) $t = 7T$ for the 2D test case of the temperature transfer during wave plunging

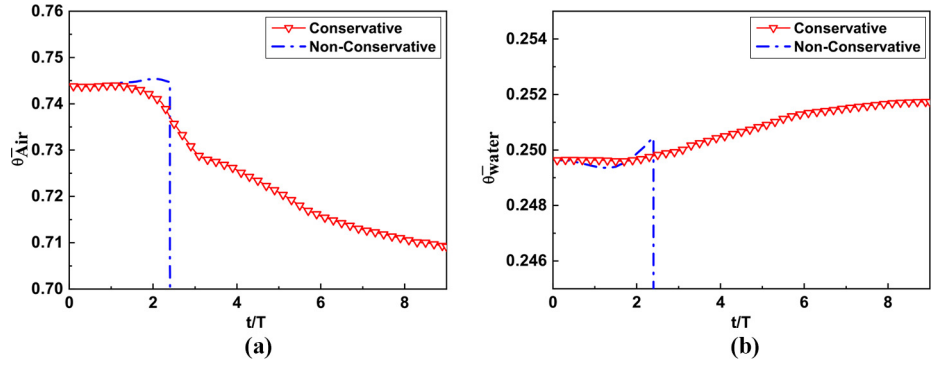

Figure 11. The evolution of the bulk mean temperature of (a) air and (b) water obtained from different $2D$ simulations by solving either conservative or non-conservative form of temperature equation

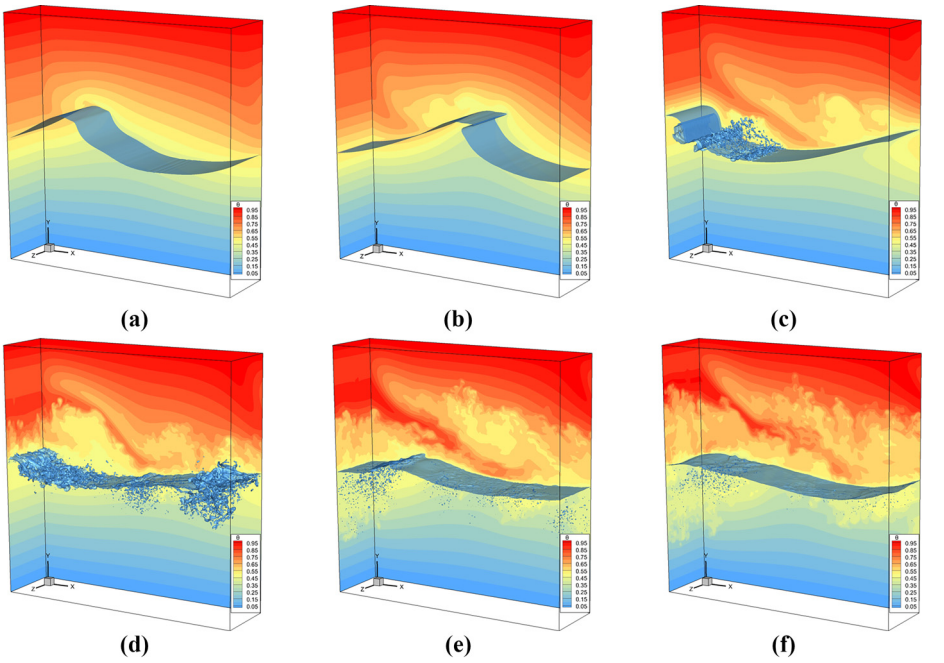

Figure 12.
Instantaneous geometry of a breaking wave and contours of temperature at (a) $t = 0.5T$, (b) $t = 1.0T$, (c) $t = 2.0T$, (d) $t = 4.0T$, (e) $t = 7.0T$ and (f) $t = 9.0T$ obtained from a three-dimensional simulation

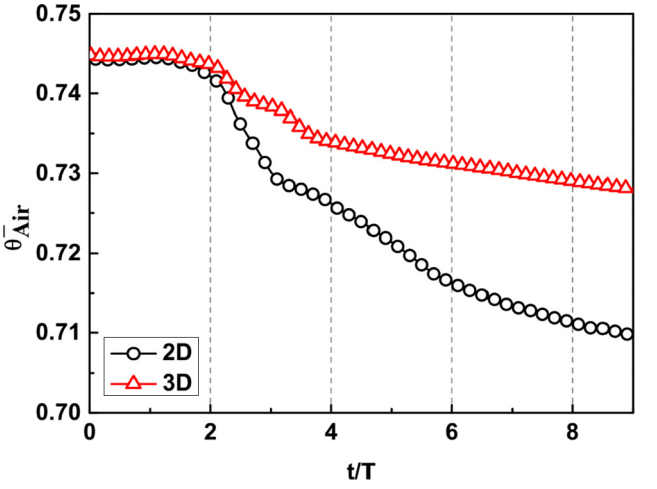

Figure 13.
Time evolution of the bulk mean temperature of air obtained from the 2D and 3D simulations

remains approximately constant before the overturning jet hits the water surface at $t = 2.0T$. After that, the temperature of air drops drastically because of the strong mixing between air and cold water. It is also seen that the decreasing rate of temperature is faster in the 2*D* case than in the 3*D* case. This observation can be attributed to the slower decaying rate of the kinetic energy in the 2*D* case than in the 3*D* case (Nas and Tryggvason, 2003). In other words,

the mixing effects induced by the wave breaking is stronger in the 2*D* simulation, which tends to enhance the heat exchange between air and water. The results shown in Figures 11 and 12 indicate that the proposed scheme is robust for numerical simulation of heat transfer in 3D two-fluid flows with high volumetric heat capacity contrasts and complex interface geometries.

4. Conclusion

In summary of this paper, we have developed a new scheme for numerical simulations of heat transfer in two-phase flows with large volumetric heat capacity variations between liquid and gas. The proposed scheme adopts the basic idea underlying the consistent transport of momentum and density (Ghods and Herrmann, 2013; Nangia *et al.*, 2019). Specifically, we solve an additional transport equation of the volumetric heat capacity along with the temperature using consistent spatial-discretization and temporal-integration schemes. The proposed scheme is first tested by isolating the advection and diffusion terms in the temperature transport equation. The advection term is tested through the case of the convection of a hot droplet with high volumetric heat capacity and the results show that a consistent discretization scheme in both time and space is crucial for a robust simulation of the heat transfer. The diffusion term is tested by conducting the case of a stationary air–water tank with temperature variation between top and bottom walls. A homogenous heat source is added in the whole computation domain. It is seen that the numerical solution converges to the analytical solution in a second-order accuracy.

To further validate the solver in problems with violent interface topology changes, we have conducted numerical simulations of heat transfer during wave plunging at high Reynolds number of $Re = 10^8$. The 2D simulation results indicate that conservative form of temperature equation are more robust than the non-conservative ones. The test of the 3D case shows that the simulation is stable and reasonably accurate when the proposed method is employed.

Finally, we note that we are not able to provide more comparison of our results with other numerical results, because released numerical simulation data at present are limited in the literature. Despite that, the accuracy of both advection and diffusion terms are verified separately against the analytical solutions and the results show that the numerical errors are acceptable for two-fluid heat transfer problem with high volumetric heat capacity contrasts at high Reynolds numbers.

References

Arrufat, T., Crialesi-Esposito, M., Fuster, D., Ling, Y., Malan, L., Pal, S., Scardovelli, R., Tryggvason, G. and Zaleski, S. (2020), "A mass-momentum consistent, volume-of-Fluid method for incompressible flow on staggered grids", *Computers and Fluids*, Vol. 215, p. 104785, doi: 10.1016/j.compfluid.2020.104785.

Aulisa, E., Manservisi, S. and Scardovelli, R. (2003), "A mixed markers and volume-of-fluid method for the reconstruction and advection of interfaces in two-phase and free-boundary flows", *Journal of Computational Physics*, Vol. 188 No. 2, pp. 611-639, doi: 10.1016/S0021-9991(03)00196-7.

Dabiri, S. and Tryggvason, G. (2015), "Heat transfer in turbulent bubbly flow in vertical channels", *Chemical Engineering Science*, Vol. 122, pp. 106-113, doi: 10.1016/j.ces.2014.09.006.

Deen, N.G. and Kuipers, J.A.M. (2013), "Direct numerical simulation of wall-to liquid heat transfer in dispersed gas-liquid two-phase flow using a volume of fluid approach", *Chemical Engineering Science*, Vol. 102, pp. 268-282, doi: 10.1016/j.ces.2013.08.025.

Desjardins, O. and Moureau, V. (2010), "Methods for multiphase flows with high density ratio", *Center for Turbulence Research Proceedings of the Summer Program*, pp. 313-322, available at: http://ctr.stanford.edu/Summer/SP10/6_02_desjardins.pdf

Ernez, S. and Morency, F. (2019), "Eulerian–Lagrangian CFD model for prediction of heat transfer between aircraft deicing liquid sprays and a surface", *International Journal of Numerical Methods for Heat and Fluid Flow*, Vol. 29 No. 7, pp. 2450-2475, doi: 10.1108/HFF-09-2018-0534.

Ghods, S. and Herrmann, M. (2013), "A consistent rescaled momentum transport method for simulating large density ratio incompressible multiphase flows using level set methods", *Physica Scripta*, Vol. T155 No. T155, doi: 10.1088/0031-8949/2013/T155/014050.

Krause, F., Schüttenberg, S. and Fritsching, U. (2010), "Modelling and simulation of flow boiling heat transfer", *International Journal of Numerical Methods for Heat and Fluid Flow*, Vol. 20 No. 3, pp. 312-331, doi: 10.1108/09615531011024066.

Liu, X.D., Fedkiw, R.P. and Kang, M. (2000), "A boundary condition capturing method for Poisson's equation on irregular domains", *Journal of Computational Physics*, Vol. 160 No. 1, pp. 151-178, doi: 10.1006/jcph.2000.6444.

Lörstad, D. and Fuchs, L. (2004), "High-order surface tension VOF-model for 3D bubble flows with high density ratio", *Journal of Computational Physics*, Vol. 200 No. 1, pp. 153-176, doi: 10.1016/j.jcp.2004.04.001.

Lu, M., Lu, J., Zhang, Y. and Tryggvason, G. (2019), "Numerical study of thermocapillary migration of a bubble in a channel with an obstruction", *Physics of Fluids*, Vol. 31 No. 6, p. 062101, doi: 10.1063/1.5094033.

Mei, C.C. (1989), *The Applied Dynamics of Ocean Surface Waves*, World scientific.

Nangia, N., Griffith, B.E., Patankar, N.A. and Bhalla, A.P.S. (2019), "A robust incompressible Navier-Stokes solver for high density ratio multiphase flows", *Journal of Computational Physics*, Vol. 390, pp. 548-594, doi: 10.1016/j.jcp.2019.03.042.

Nas, S. and Tryggvason, G. (2003), "Thermocapillary interaction of two bubbles or drops", *International Journal of Multiphase Flow*, Vol. 29 No. 7, pp. 1117-1135, doi: 10.1016/S0301-9322(03)00084-3.

Nas, S., Muradoglu, M. and Tryggvason, G. (2006), "Pattern formation of drops in thermocapillary migration", *International Journal of Heat and Mass Transfer*, Vol. 49 Nos 13/14, pp. 2265-2276, doi: 10.1016/j.ijheatmasstransfer.2005.12.009.

Panda, A., Weitkamp, Y.E.J., Rajkotwala, A.H., Peters, E.A.J.F., Baltussen, M.W. and Kuipers, J.A.M. (2019), "Influence of gas fraction on wall-to-liquid heat transfer in dense bubbly flows", *Chemical Engineering Science: X*, Vol. 4, doi: 10.1016/j.cesx.2019.100037.

Park, I.K., Park, I.K., Cho, H.K., Yoon, H.Y. and Jeong, J.J. (2009), "Numerical effects of the semi-conservative form of momentum equations for multi-dimensional two-phase flows", *Nuclear Engineering and Design*, Vol. 239 No. 11, pp. 2365-2371, doi: 10.1016/j.nucengdes.2009.06.011.

Patel, J.K. and Natarajan, G. (2017), "A novel consistent and well-balanced algorithm for simulations of multiphase flows on unstructured grids", *Journal of Computational Physics*, Vol. 350, pp. 207-236, doi: 10.1016/j.jcp.2017.08.047.

Raessi, M. and Pitsch, H. (2012), "Consistent mass and momentum transport for simulating incompressible interfacial flows with large density ratios using the level set method", *Computers and Fluids*, Vol. 63, pp. 70-81, doi: 10.1016/j.compfluid.2012.04.002.

Rudman, M. (1998), "A volume-tracking method for incompressible multifluid flows with large density variations", *International Journal for Numerical Methods in Fluids*, Vol. 28 No. 2, pp. 357-378, doi: 10.1002/(SICI)1097-0363(19980815)28:2<357::AID-FLD750>3.0.CO;2-D.

Scardovelli, R. and Zaleski, S. (1999), "Direct numerical simulation of free-surface and interfacial flow", *Annual Review of Fluid Mechanics*, Vol. 31 No. 1, pp. 567-603, doi: 10.1146/annurev.fluid.31.1.567.

Shin, S. and Juric, D. (2009), "A hybrid interface method for three-dimensional multiphase flows based on front tracking and level set techniques", *International Journal for Numerical Methods in Fluids*, Vol. 60 No. 7, pp. 753-778, doi: 10.1002/fld.1912.

Sussman, M. and Puckett, E.G. (2000), "A coupled level set and volume-of-fluid method for computing 3d and axisymmetric incompressible two-phase flows", *Journal of Computational Physics*, Vol. 162 No. 2, pp. 301-337, doi: 10.1006/jcph.2000.6537.

Sussman, M., Smereka, P. and Osher, S. (1994), "A level set approach for computing solutions to incompressible two-phase flow", *Journal of Computational Physics*, Vol. 114 No. 1, pp. 146-159, doi: 10.1006/jcph.1994.1155.

Sussman, M., Smith, K.M., Hussaini, M.Y., Ohta, M. and Zhi-Wei, R. (2007), "A sharp interface method for incompressible two-phase flows", *Journal of Computational Physics*, Vol. 221 No. 2, pp. 469-505, doi: 10.1016/j.jcp.2006.06.020.

Tanaka, M. (2011), "Numerical study on flow structures and heat transfer characteristics of turbulent bubbly upflow in a vertical channel", *Computational Simulations and Applications*, Vol. 20 No. 1, pp. 119-142, doi: 10.5772/24405.

Tryggvason, G., Scardovelli, R. and Zaleski, S. (2011), "Direct numerical simulations of Gas-Liquid multiphase flows", *Direct Numerical Simulations of Gas-Liquid Multiphase Flows*, Vol. 9780521782, pp. 1-324, doi: 10.1017/CBO9780511975264.

Ubbink, O. and Issa, R.I. (1999), "A method for capturing sharp fluid interfaces on arbitrary meshes", *Journal of Computational Physics*, Vol. 153 No. 1, pp. 26-50, doi: 10.1006/jcph.1999.6276.

Unverdi, S.O. and Tryggvason, G. (1992), "A front-tracking method for viscous, incompressible, multi-fluid flows", *Journal of Computational Physics*, Vol. 100 No. 1, pp. 25-37, doi: 10.1016/0021-9991(92)90307-K.

Wan, Z., Wang, X., Zhu, J. and Yang, M. (2015), "Numerical simulation of a diurnal cycle on the structure of ocean mixed layer", *International Journal of Numerical Methods for Heat and Fluid Flow*, Vol. 25 No. 7, pp. 1514-1524, doi: 10.1108/HFF-05-2014-0122.

Wang, D., Qiang, H. and Shi, C. (2020), "A multiphase SPH framework for solving the evaporation and combustion process of droplets", *International Journal of Numerical Methods for Heat and Fluid Flow*, Vol. 30 No. 3, pp. 1547-1575, doi: 10.1108/HFF-08-2019-0666.

Yan, Y.Y. and Li, W.Z. (2006), "Numerical modelling of a vapour bubble growth in uniformly superheated liquid", *International Journal of Numerical Methods for Heat and Fluid Flow*, Vol. 16 No. 7, pp. 764-778, doi: 10.1108/09615530610683502.

Yang, Z., Lu, M. and Wang, S. (2021), "A robust solver for incompressible high-Reynolds-number two-fluid flows with high density contrast", *Journal of Computational Physics*, Vol. 441, p. 110474, doi: 10.1016/j.jcp.2021.110474.

Yin, Z. and Li, Q. (2015), "Thermocapillary migration and interaction of drops: two non-merging drops in an aligned arrangement", *Journal of Fluid Mechanics*, Vol. 766 No. March, pp. 436-467, doi: 10.1017/jfm.2015.10.

Zhu, L. and Masud, A. (2021), "Variationally derived interface stabilization for discrete multiphase flows and relation with the ghost-penalty method", *Computer Methods in Applied Mechanics and Engineering*, Vol. 373, p. 113404, doi: 10.1016/j.cma.2020.113404.

Zuzio, D., *et al.* (2020), "A new efficient momentum preserving Level-Set/VOF method for high density and momentum ratio incompressible two-phase flows", *Journal of Computational Physics*, Vol. 410, p. 109342, doi: 10.1016/j.jcp.2020.109342.

Corresponding author
Zixuan Yang can be contacted at: yangzx@imech.ac.cn